Materials Today Communications 47 (2025) 113124

Contents lists available at ScienceDirect

Materials Today Communications

journal homepage: www.elsevier.com/locate/mtcomm

Comparison and evolution of Ti6Al4V bioalloy fabricated by laser and electron beam additive manufacturing: Mechanical features and anisotropic electrochemical properties

Parinaz Mofazali [a], Masoud Atapour [a,*], Ozkan Gokcekaya [b], Sung-Hyun Park [b], Batur Ercan [c,d,e], Takayoshi Nakano [b]

[a] Department of Materials Engineering, Isfahan University of Technology, Isfahan 84156-83111, Iran
[b] Anisotropic Design & Additive Manufacturing Research Center, The University of Osaka, 2-1 Yamadaoka, Suita, Osaka 565-0871, Japan
[c] Department of Metallurgical and Materials Engineering, Middle East Technical University, Çankaya, Ankara 06800, Türkiye
[d] Biomedical Engineering Program, Middle East Technical University, Çankaya, Ankara 06800, Türkiye
[e] BIOMATEN, Center of Excellence in Biomaterials and Tissue Engineering, Middle East Technical University, Çankaya, Ankara 06800, Türkiye

ARTICLE INFO

Keywords:
Ti6Al4V
SLM
EBM
Anisotropy
Corrosion
Biomedical

ABSTRACT

With current technology, most biomedical implants are made using metal-based alloys, with a growing preference for metal additive manufacturing (AM) to achieve customized properties. Therefore, this study investigated Ti-6Al-4V (Ti64) alloys produced using two common AM techniques: electron beam melting (EBM) and selective laser melting (SLM). The aim is to compare the microstructure, mechanical properties, and anisotropy electrochemical corrosion behavior of Ti64 samples scanned with SLM-XX, SLM-XY, and EBM-XX strategies. Surface roughness, microstructure, and microhardness tests were conducted to establish correlations with the manufacturing process and surface characteristics. Optical and scanning electron microscopy microstructural analysis revealed notable variations influencing mechanical performance. Moreover, anisotropy-assessing electrochemical corrosion evaluations showed that SLM samples exhibited superior corrosion resistance compared to EBM samples. Notably, the (YZ) planes in the SLM-XY sample demonstrated the highest corrosion resistance (R_{ct} $\sim 4.45 \times 10^6$ $\Omega.cm^2$), attributed to reduced dislocation density and enhanced passivation. Furthermore, results showed that the method of fabrication affected the wettability of Ti64 alloys. The SLM-XY samples exhibited the lowest water contact angle (84.45°), whereas the EBM samples showed the highest (99.87°). Finally, bioactivity assessments after 21 days in simulated body fluid (SBF) revealed no cracking or surface damage in any of the tested samples. The formation of calcium- and phosphorus-rich deposits indicates their potential suitability for orthopedic applications.

1. Introduction

The unique properties of Ti-6Al-4V (Ti64), including its remarkable biocompatibility, high strength, and low weight, make it ideal for implants and prostheses. Its usage in biomedical additive manufacturing is crucial due to these characteristics. AM is now a cutting-edge biomedical manufacturing technique that significantly affects dentistry and medicine [1]. Several industries outside of biomedical applications have profited from AM technology, such as aerospace [2], automotive [3], and architecture [4]. It is difficult to create metallic implants with complex, patient-specific shapes using traditional production methods, but advanced additive manufacturing techniques enable the creation of such implants. These developments have enhanced the performance and customization of medical equipment [5]. Traditional design is rarely necessary because additive manufacturing can develop complex geometries that are impossible to produce through conventional methods [6]. Recent progress in implant customization has been driven by the development of AM methods, which enable the production of fully dense metal components with adjustable Young's modulus [7,8]. One of the key benefits of AM is its capacity to produce materials with a variety of crystallographic phases. These structures were previously only possible to fabricate through post-thermo-mechanical processing in traditional manufacturing [9]. Among the AM techniques standardized in ISO/ASTM 52900, powder bed fusion (PBF) is widely used for metal

---

* Corresponding author.
E-mail address: m.atapour@cc.iut.ac.ir (M. Atapour).

https://doi.org/10.1016/j.mtcomm.2025.113124
Received 29 January 2025; Received in revised form 9 June 2025; Accepted 16 June 2025

fabrication [10]. PBF is divided into two groups based on the type of energy source: Selective Laser Melting (SLM), which employs a strong laser, and Electron Beam Melting (EBM), which uses an electron beam in a vacuum chamber [11]. Materials such as titanium, stainless steel, aluminium, and cobalt-based alloys have been produced using SLM and EBM processes. Numerous studies have been conducted on their mechanical characteristics, microstructure, and potential applications [12–14]. Compared to other metallic implant materials, it also has superior hardness, a considerably lower density, and outstanding corrosion resistance [15]. Ti64 components fabricated by SLM and EBM have proven to be highly useful in various industries, particularly in medical applications such as dental and orthopedic prostheses [16,17], primarily due to their favorable chemical and mechanical properties [18,19]. Since AM components are built layer by layer, their microstructure and properties are strongly influenced by scanning strategies and processing parameters [20,21]. This work aims to investigate and compare the properties of Ti64 bulk materials manufactured using SLM and EBM, depending on scanning strategy and process parameters. Thus, it is important to investigate the electrochemical behavior of Ti64 produced by AM under various build techniques, as these may result in anisotropic material properties across different production planes (YZ, XZ, XY), which can alter the long-term dependability and electrochemical stability of Ti64 implants in biomedical applications.

2. Materials and methods

Ti64 samples were produced using two different machines: an SLM system (EOS M290, EOS, Germany) and an EBM system (Arcam Q10, Arcam AB, GE Additive). Both machines utilized standard Ti64 ELI powders with high sphericity (~1) provided by the equipment manufacturer, following the ASTM F3001–14. To prevent oxidation during fabrication, the oxygen level in the construction chamber was maintained below 100 ppm during the SLM process. In the EBM process, the powder was preheated to 540°C, and a vacuum of 4×10^{-3} mbar was maintained, with helium as the regulating gas. A highly focused electron beam (focus offset = 0) was applied for Ti64 fabrication. The main process parameters for the SLM and EBM methods are detailed in Table 1. For the comparison between SLM and EBM, the laser absorption efficiency of Ti64 (approximately 70 %) was taken into account as reported in our previous study [22]. Fig. 1 illustrates the principles of SLM and EBM processes with the build stage design for Ti64 fabrication and how the XX and XY scanning strategies define the scan path during the AM process, influencing the resulting microstructure and mechanical propertiest (Table 2).

Samples for microstructural investigations and various experiments were prepared by EDM cutting from a sample size of $1 \times 1 \times 1$ cm^3 after removal of support structure for the observation plane in interest. They were then sequentially polished using P600, P800, P1200, P2400, and P5000 sandpapers, followed by final polishing in an Al_2O_3 suspension to achieve a mirror-like surface, and then etched in a solution containing 4 vol% HF, 6 vol% HNO_3, and 90 vol% H_2O. Microstructural and compositional characterizations were performed using optical microscopy (OM, Zeiss Axiolab) and scanning electron microscopy (SEM, Philips XI30) equipped with an energy-dispersive X-ray spectrometer (EDS). Detailed microstructural analyses were conducted using an electron backscatter diffraction (EBSD) system (NordlysMax3, Oxford Instruments, UK) attached to the FE-SEM. Data collection was carried out using Aztec software (Oxford Instruments, UK), while Channel 5 software (Oxford Instruments, UK) was employed for data processing. The crystal structure of the samples was examined using X-ray diffraction (XRD, PMD Philips X-Pert, Netherlands) with a Cu-Kα radiation source. The scanning rate was 0.05º per 4 s, covering a range from 20º to 80º. Before performing the electrochemical tests, the samples were polished and subjected to ultrasonic cleaning in acetone, ethanol, and distilled water for 15 min. Corrosion experiments were conducted in a 1 M HCl solution at 25°C, using an Ag/AgCl reference electrode, a platinum wire counter electrode, and a Ti64 sample as the working electrode. The electrochemical assessments included open-circuit potential (OCP), potentiodynamic polarization, and electrochemical impedance spectroscopy (EIS). A commercial electrochemical analyzer was used to evaluate the electrochemical properties of SLM (XY, XX) and EBM samples along their (-x, -y, and -z) planes, with tests conducted at least three times to ensure data reliability. OCP experiments were performed before other tests to stabilize the OCP in the solution, enabling potentiostatic EIS measurements. The potentiodynamic polarization curves were recorded at a scan rate of 10 mV/s over a potential range of -2 V to $+2$ V relative to the open-circuit potential. Electrochemical impedance spectroscopy measurements were performed at open-circuit potential, using an AC amplitude of 5 mV and a frequency range of 10 mHz to 10 kHz. The relative densities of the SLM and EBM samples were determined using the standard Archimedes method. The specimen mass was measured separately at room temperature and recorded as m_a (in air) and m_w (in water). Using the density of water (ρ_{water}=1), the density of the Ti64 specimens (ρ_A) was calculated using the following equations [23]:

$$\rho_A = \frac{m_a}{m_a - m_w}\rho_w \tag{1}$$

$$P(\%) = (1 - \frac{\rho_{bulk}}{\rho_{theoretical}}) \times 100 \tag{2}$$

Ultrapure water static tests were conducted to measure the contact angle (CA) of the samples. A 5 µL droplet was applied to the surface, and the CA was immediately recorded at 25°C, with at least three measurements taken. Surface roughness was quantified using the stylus contact method with a portable surface roughness tester (Mitutoyo SJ-210). Three measurements were taken from each sample, with a 120° rotation between each measurement, and the stylus traversed perpendicularly to the layer borders. Microhardness was assessed on the lateral surface of the EBM and SLM Ti64 substrates using a Mitutoyo Micro Vickers hardness tester under a 0.2 kgf force for 10 s. The Vickers microhardness (HV) was calculated for each indentation using the mean of the diagonals (d) and the applied load (F) [24]. Roughness and microhardness measurements were performed at multiple locations across the sample surface, with at least three indentations made per sample to ensure accuracy and repeatability.

$$HV = \frac{1.8544F}{d^2} \tag{3}$$

The bioactivity of the SLM XX, SLM XY, and EBM XX Ti64 samples was assessed by immersing them in 40 mL of 1X simulated body fluid (SBF) at 37°C for 21 days. The 1X SBF solution was prepared following the Kokubo protocol [25]. SEM and EDS analyses were conducted to evaluate the formation of calcium-containing minerals on the specimens after 21 days of immersion in SBF.

Table 1
Parameters used for the fabrication of the samples.

Parameter set	Scan strategy	Power (mW)	Scan Speed (mm/s)	Hatch distance (mm)	Layer thickness (mm)	Energy Density (J/mm^3)
SLM-XY scan	XY scan	360	1200	0.030	0.06	166.7
SLM-X scan	XX scan	360	1200	0.100	0.06	50.0 (70 % efficiency= 35.0)
EBM-X scan	XX scan	450	2500	-	0.05	36.0

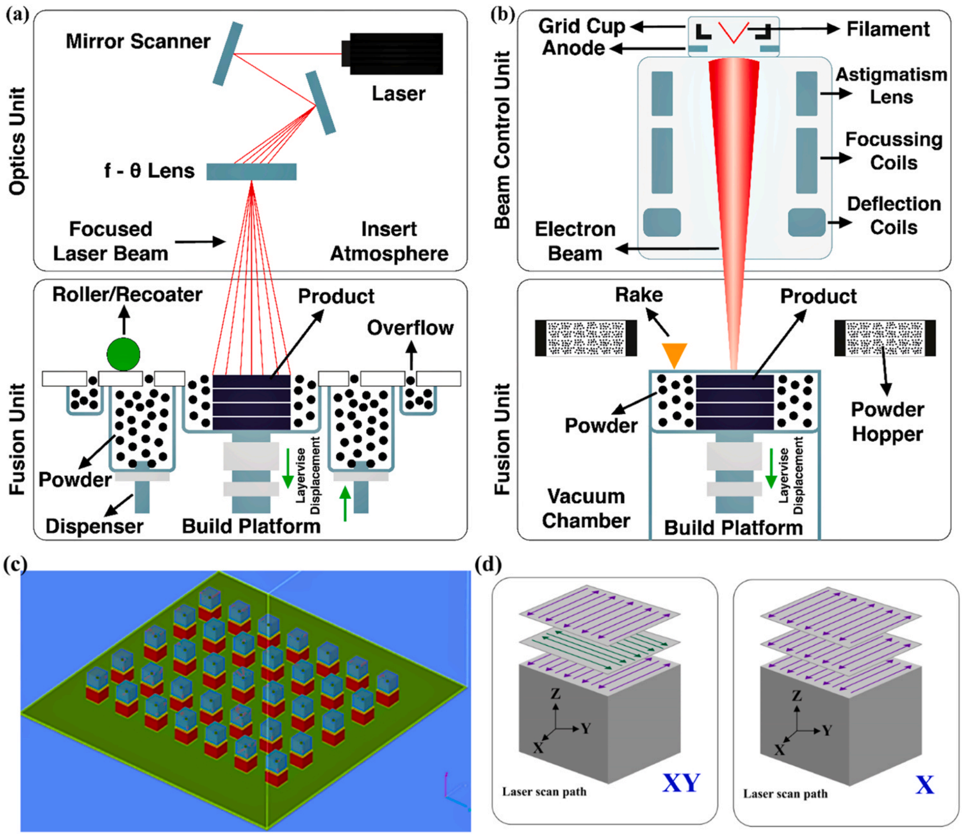

Fig. 1. Schematics of (a) SLM and (b) EBM processes (c) with the design of cube Ti64 samples on the build stage by materialise magics, and (d) bidirectional scan strategies: XY and X scan strategies.

Table 2
Abbreviation list of the samples.

Scan strategy	Planes	Abbreviation
SLM-XY scan	YZ	SLM XY-x
	XZ	SLM XY-y
	XY	SLM XY-z
SLM-XX scan	YZ	SLM XX-x
	XZ	SLM XX-y
	XY	SLM XX-z
EBM-XX scan	YZ	EBM XX -x
	XZ	EBM XX -y
	XY	EBM XX -z

3. Results and discussion

3.1. Phase characterization

Fig. 2 displays the XRD patterns of the Ti64 samples produced by EBM XX and SLM (XX, XY). The majority of the peaks in both samples can be attributed to the α/α′ phase. It is difficult to distinguish between α and α′ because of their similar lattice characteristics and shared HCP structure. The BCC β-phase peak is also seen in the EBM samples as a result of the high preheat conditions. SLM samples exhibited a finer phase compared to EBM samples, as evidenced by the broader α/α′ peaks in the former. The presence of both HCP and BCC diffraction spots in the EBM samples confirms the coexistence of the α and β phases. The obtained XRD patterns are consistent with those reported in previous studies [26,27]. Although Ti64 is a common dual-phase (α + β) alloy, the peaks of the β phase are not visible in the SLM samples. However, the SLM samples have the acicular fine α′ phase, and the rapid cooling that occurs during the manufacturing process causes the β structures to change into martensitic structures [28].

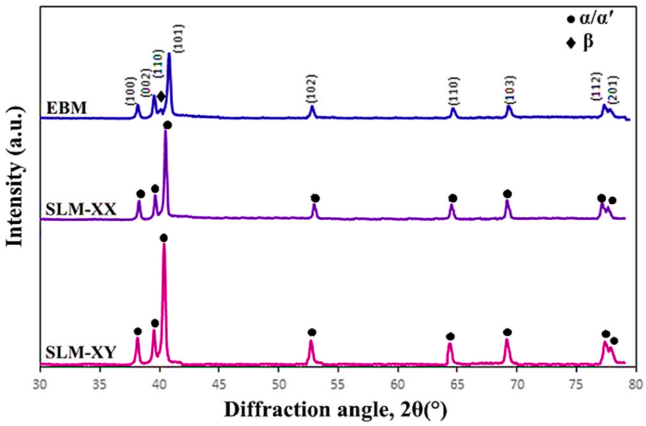

Fig. 2. The XRD patterns of (a) SLM -XY, (b) SLM- XX, and (c) EBM XX samples.

3.2. Microstructure characterization

The microstructures of the SLM (XY, XX) and EBM XX samples, as observed by optical and scanning electron microscopy, are shown in Figs. 3 and 4. As shown in Fig. 3(a), the adjusted AM processing parameters significantly decrease the quantity and size of pores [29], improving densification. Chessboard-like microstructural features are frequently detected when a specimen is produced using the cross-hatching laser scanning technique [30,31], which was also recognizable in our samples due to the use of this process.

Fig. 4(a) shows the acicular α′ martensite transformed from the columnar parent β phase, while Fig. 4(b) illustrates the transition of the original columnar β grains into acicular α′ martensite. The parallel

Fig. 3. The OM images of the (a) SLM-XY, (b) SLM-XX, and (c) EBM XX samples.

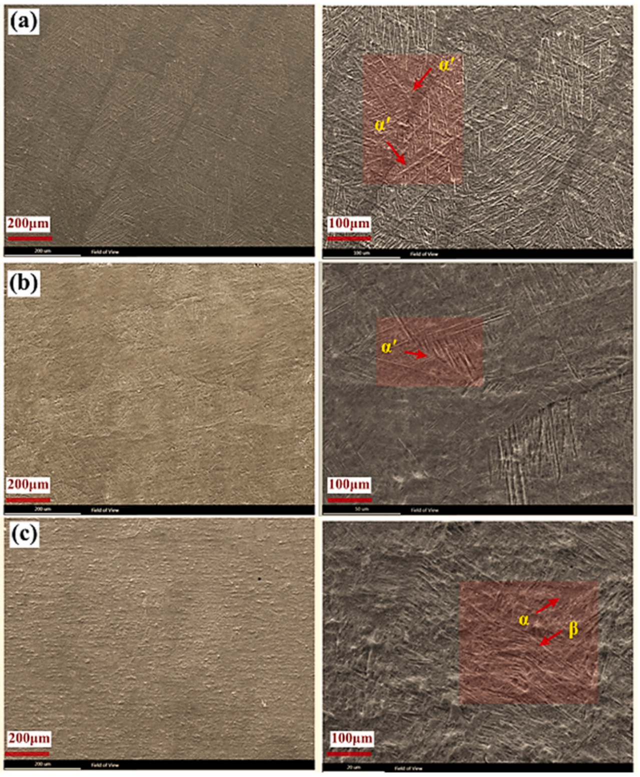

Fig. 4. SEM micrographs of the (a) SLM-XY, (b) SLM-XX, and (c) EBM samples.

columnar shape of the initial β grains clearly follows the build direction. It is well established that this columnar structure forms due to the epitaxial growth of the original β phase grains during the layer-by-layer deposition process, followed by directional cooling along the build direction. The metal printed by EBM initially solidifies into columnar β grains that grow along the build direction (Fig. 4c). This microstructure consists of α laths and β ribs, as shown in Fig. 4(c). As the printed parts cool, the β grain boundaries act as nucleation sites for α grains, and the initial β phase within the grains transforms into α/β lamellar structures [32]. However, remnants of the previous β columnar grain boundaries can be seen in both cases, suggesting that the Ti64 alloy's primary solidification mode is unaffected by the production technique. The final microstructure of the material is largely determined by the rate of cooling through the beta transus temperature, where the β phase starts to change into other phases like α or martensite [33]. While slower cooling tends to produce coarser structures with a greater presence of the α phase or other equilibrium phases, rapid cooling of the β phase can result in a finer microstructure, possibly incorporating martensite [34].

3.3. EBSD analysis

The microstructural characteristics, including grain orientation and size, residual stress, and recrystallization, significantly affect the corrosion properties. Therefore, EBSD observations were conducted to investigate the microstructural details of the samples. Fig. 5 presents the inverse pole figures for each plane (YZ, XZ, and XY) and the pole figures of the XY plane for the AM Ti64 samples. Grain orientation in the observation area for the SLM XY at the YZ cross-section was strongly selected, indicating that the epitaxially grown parent β phase (tilted towards the scan track direction due to the small hatch spacing altering the thermal gradient direction) resulted in a set of α grains with similar orientations. Although this selection was not identified in the XZ and XY planes, the relatively strong α grain orientation in the YZ plane for SLM XY was attributed to the strong crystallographic texture development, as indicated by the highest multiple of uniform distribution (MUD) values, 25.5 for parent β grains (Ti-Cubic) and 22.1 for child α grains (Ti-Hex). The β → α phase transformation follows the Burgers orientation relationship (BOR): (0001)α // (110)β, [11-20]α // [111]β. Considering BOR, there are 12 possible α grain variations. As shown in the pole figure results, the parent β phase formed a fiber texture, resulting in variations in β grain orientation and consequently leading to a random selection of α grain orientation. However, it is crucial to highlight that controlling the selection of α variations could enhance mechanical properties in an anisotropic manner [35]. The SLM XX sample exhibited locally selected α grains corresponding to the orientation of parent β grains according to BOR in the YZ plane. However, this selection was limited to epitaxially grown singular β grains, while neighboring grains displayed different α grain selections due to variations in parent β grain orientation. Additionally, the SLM XX condition led to longer α grains compared to SLM XY, which was expected due to the single-directional scan (XX scan) promoting α grain growth. However, due to the low laser energy density of SLM XX, there was no significant texture development, as shown in the pole figures, with the lowest MUD values for β and α grains. The microstructural characteristics of EBM XX were similar to those of SLM XY in terms of the parent β phase, forming a fiber texture and resulting in random α selection from the 12 variations according to BOR. This similarity may be attributed to the impact of heat accumulation from the high energy density and small hatch distance of SLM XY, whereas the EBM process was performed under a high preheat temperature. Park et al. [33] discussed the advantage of a small hatch distance in accumulating heat and enhancing texture formation in β-solidifying TiAl alloys. Regarding the corrosion behavior of alloys, it has been widely reported that smaller grains are more susceptible to corrosion in a corrosive environment [36]. The XY (-z) plane exhibited a smaller average grain size compared to the YZ (x-direction) and XZ (-y) planes in samples fabricated via the EBM, SLM-XY, and SLM-XX processes. This is because the YZ and XZ planes are prone to forming columnar grains due to epitaxial growth. Anisotropic corrosion resistance occurs due to differences in passivation behavior, meaning that some crystallographic planes may resist corrosion better than others due to more effective passivation [37,38]. Owing to the evenly distributed temperature during the process, EBM XX exhibited minimal differences in grain size across different planes. In contrast, the grain size of each plane in the SLM samples varied depending on the epitaxial grain growth direction, which was affected by the scan strategy and laser energy density, as shown in Fig. 6.

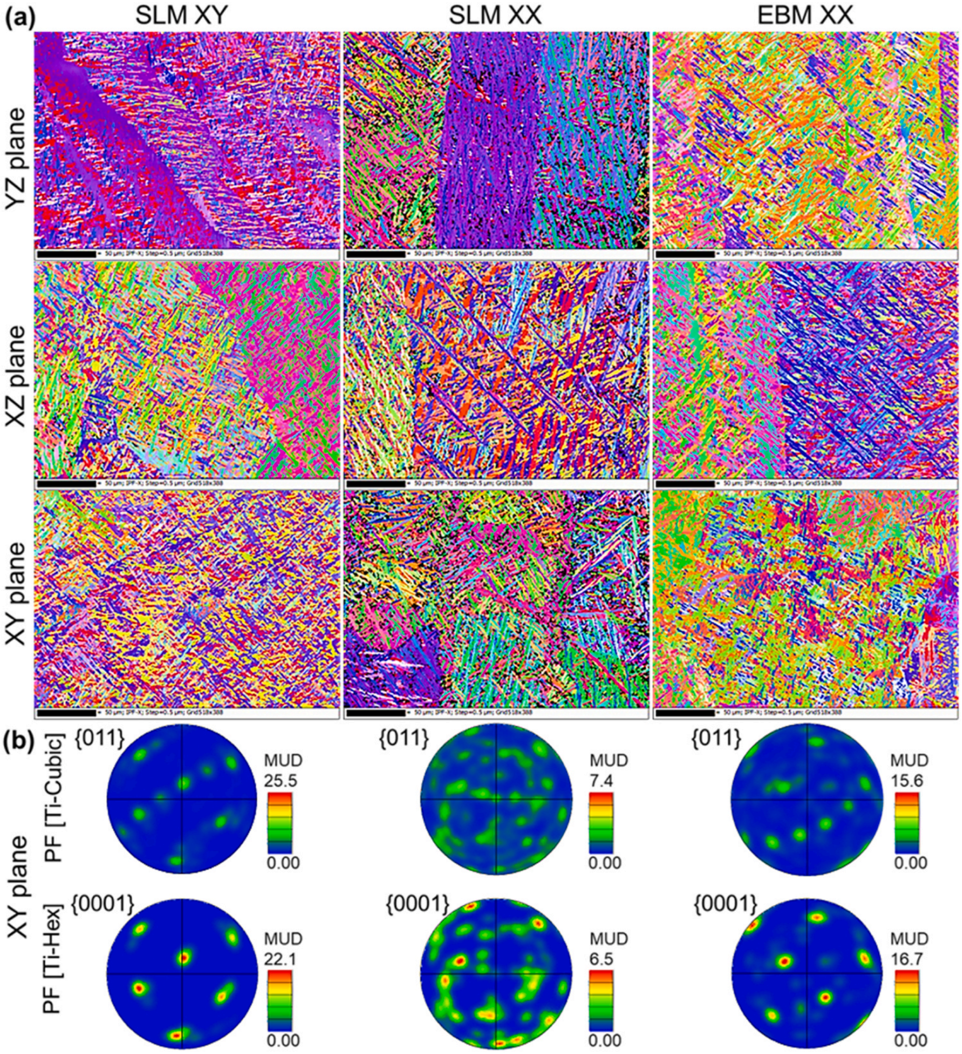

Fig. 5. EBSD analyses of the SLM-XY, SLM-XX, and EBM ssamples for grain orientation characteristics: (a) Inverse pole figure maps and (b) pole figures of α and β phases with corresponding MUD values.

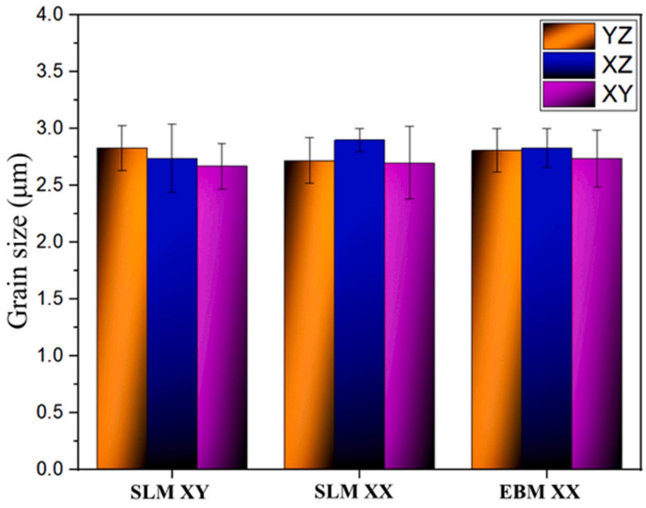

Fig. 6. Average grain size of each sample and each surface obtained from the EBSD observations.

It can be observed from Fig. 7 that the average KAM of the XY plane is higher than that of the YZ and XZ planes in both SLM and EBM samples, indicating a greater degree of misorientation and suggesting higher residual stress accumulation within the grains [39]. The average KAM values were similar between the YZ and XZ planes in EBM. However, in the SLM-XY and SLM-XX samples, the average KAM values were higher in the XZ plane compared to the YZ plane, which is likely caused by the directional gas flow altering the cooling rate depending on the scan direction [40]. The quantitative analysis of Kernel Average Misorientation is used to estimate dislocation density, which is indicative of residual stress [41]. According to the average KAM distribution values in Fig. 7(b), the SLM-XX sample exhibited the highest average residual stress on each plane due to the bidirectional (X-scan) strategy and lower laser energy density. The blue region, which represents a large proportion of the sample, indicates low internal misorientation and minimal defects, while the green region is concentrated at the grain boundaries of the α′ and β phases, signifying significant local strain and high defect density areas. This distribution suggests that the grain boundary (GB) has a higher dislocation density in the EBM-XX and SLM-XX samples [42]. This is particularly concerning in terms of corrosion performance, as grain boundaries and high-stress locations are more susceptible to corrosion [43].

The grain boundaries, due to their anodic influence compared to the grain interior, are more susceptible to corrosion during immersion.

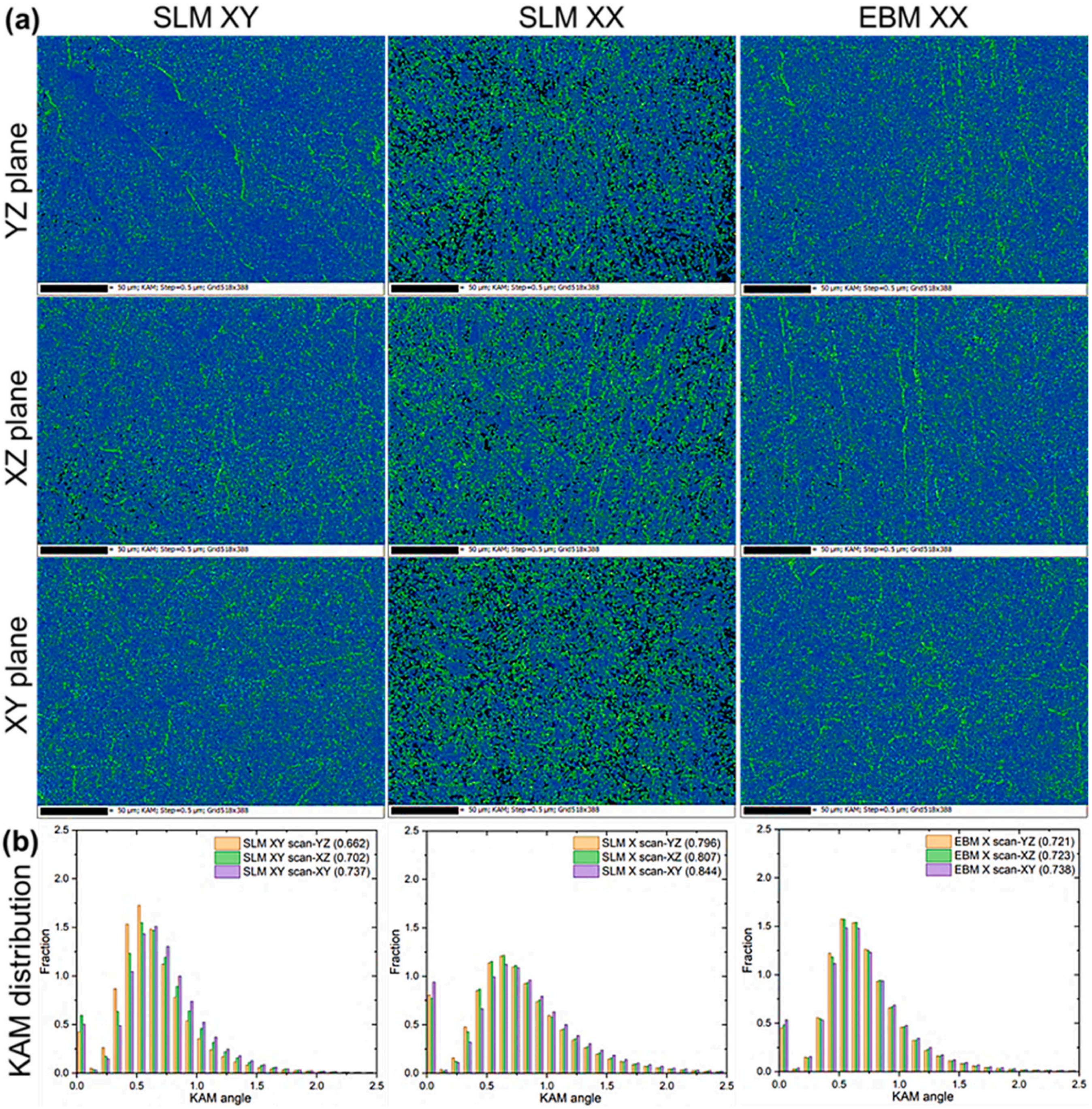

Fig. 7. EBSD analyses of the SLM-XY, SLM-XX, and EBM-XX samples for Kernel average misorientation (KAM): (a) KAM maps and (b) KAM distribution given as fraction.

However, passivation can reduce corrosion as the grain size decreases [44]. The KAM values indicate that the accumulated dislocation density contributes to an increased susceptibility to corrosion. It is worth mentioning that variations in different planes and the type of processing influence the dislocation density and residual strain in the material, which are associated with the KAM values. The density of geometrically necessary dislocations (ρ_{GND}) was analyzed in various directions for each method. In all samples, the XZ and XY planes exhibit an increase in GND density. Higher GND density in grains is associated with larger dislocation densities and higher stored energy, which can create conditions for metal corrosion. According to the recrystallized fraction map obtained via EBSD (Fig. 8), blue regions indicate recrystallized grains, while red and yellow regions represent deformed and substructured grains, respectively. From Fig. 8, it can be observed that the recrystallized, substructured, and deformed regions of the samples range from 17–32 %, 14–27 %, and 41–64 %, respectively. The recrystallization volume fractions of EBM-XX and SLM-XY samples were similar, whereas the SLM-XX sample exhibited a lower recrystallized phase fraction. The deformed volume fraction of the EBM sample was the lowest due to the lower cooling rate and high preheat temperature (540 °C), and it gradually increased in the order of SLM-XY and SLM-XX, which had a preheat temperature of 80 °C [45]. The volume fraction of recrystallization significantly influences the corrosion behavior of a material. Higher recrystallization volume fractions typically result in a more uniform microstructure, replacing deformed and heterogeneous regions with new, strain-free, and uniformly distributed grains [46]. This uniformity

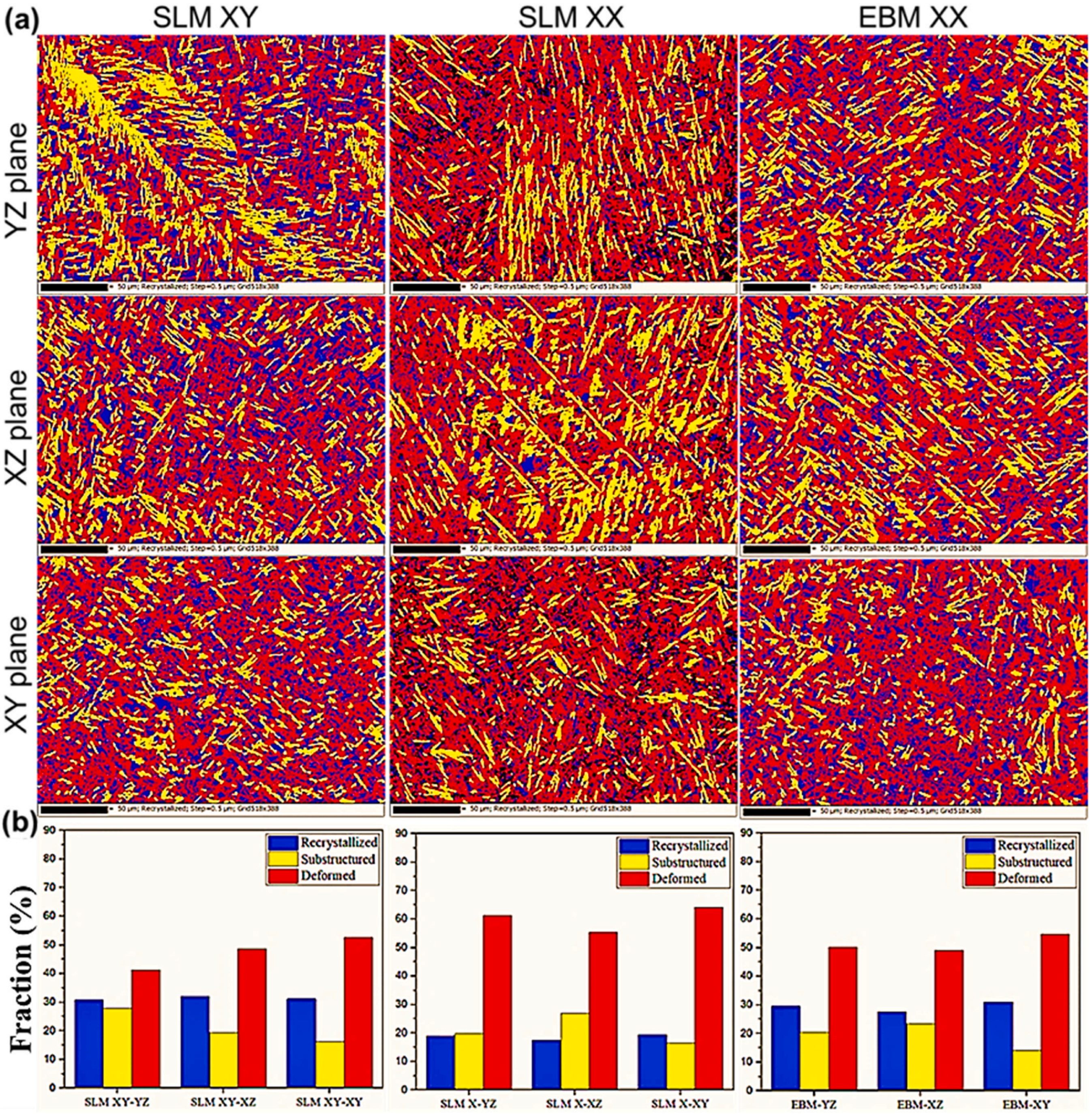

Fig. 8. EBSD analyses of the SLM-XY, SLM-XX, and EBM-XX samples for grain characteristics: (a) Recrystallization maps and (b) the distribution of grain characteristics in percentage (%).

helps mitigate localized corrosion, such as pitting, by evenly distributing electrochemical activity across the surface. Additionally, recrystallized grains contain fewer dislocations and lower internal stress, leading to reduced defect densities and fewer sites for corrosion initiation. Consequently, as the recrystallization volume fraction increases, the material exhibits greater corrosion resistance. Furthermore, a higher recrystallization volume fraction enhances the formation and durability of the passivation layer [47], facilitating the development of a compact and well-adhered oxide layer, effectively shielding the underlying metal from corrosion [48].

3.4. Electrochemical analysis

The polarization curve can be used to interpret various corrosion metrics, including corrosion potential (E_{corr}), corrosion current density (I_{corr}), and corrosion resistance (R_p). Each corrosion criterion is significant for evaluating corrosion resistance. Fig. 9 presents the potentiodynamic polarization behavior of SLM samples with varying orientations, along with Ti64 fabricated using EBM. Before conducting the polarization tests, adequate time was allowed for the OCP to stabilize. The corrosion parameter data are presented in Table 3. The R_p values were also determined using the Stern-Geary equation [49], as shown in Eq. (4):

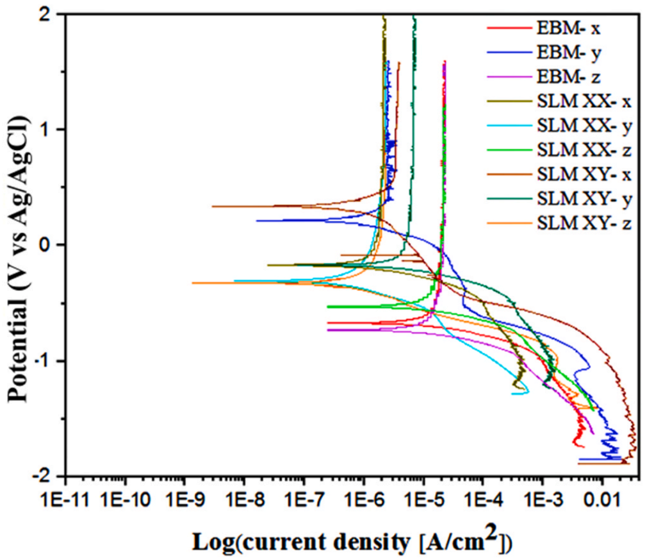

Fig. 9. Potentiodynamic polarization plots of the samples.

Table 3
Corrosion potential, corrosion current density, and polarization resistance of the Ti64 samples.

Sample	$E_{cor.}$ (V vs. SCE)	$I_{cor.}$ (A.cm^2)	R_p (Ω)
EBM XX- (YZ)	−0.6938	2.20E−05	2.37E+ 03
EBM XX- (XZ)	0.1962	1.885E−06	5.25E+ 04
EBM XX- (XY)	−0.7492	1.63E−05	3.30E+ 03
SLM XX- (YZ)	−0.3223	7.48E−07	1.16E+ 05
SLM XX- (XZ)	−0.1837	9.31E−07	1.14E+ 05
SLM XX- (XY)	−0.5415	6.24E−06	1.45E+ 04
SLM XY- (YZ)	0.3152	7.66E−07	6.39E+ 04
SLM XY- (XZ)	−0.1788	1.90E−06	3.84E+ 04
SLM XY- (XY)	−0.3357	9.60E−07	9.80E+ 04

$$R_p = \frac{\beta_a\beta_c}{2.303\quad(\beta_a+\beta_c)I_{corr}} \tag{4}$$

It is evident that each polarization curve consists of both cathodic and anodic branches, with some variations in the anodic polarization curves. This suggests that oxidation reactions occurred on their surfaces, where titanium forms a passive TiO_2 layer that protects the surface from further corrosion. All the samples in the solution exhibit a respectable level of corrosion resistance. The SLM XY-YZ (-x), SLM XX-YZ (-x), and SLM XX-XZ (-y) samples demonstrate superior corrosion resistance compared to the other samples, according to the test results. The higher I_{corr} value observed together with the lower E_{corr} values of the EBM XX-XY (−z), EBM XX-YZ (−x), and SLM XX-XY (−z) samples compared to the others, indicates that these samples exhibit poor corrosion resistance. According to the potentiodynamic curves, a passive film forms on the alloy during the anodic potential range, which suggests that the formation of this film inhibits Cl^- attack on the samples [50]. Generally, during the passivation process, a dense passive film forms closely on the metal surface, thereby slowing down the corrosion reaction [51]. The grain structure of Ti64, particularly the proportion of different grain types, plays a crucial role in its electrochemical corrosion behavior. For instance, the balance between α and β phases affects both the alloy's mechanical properties and its resistance to corrosion. The grain structure beneath the surface of Ti64 influences the stability and uniformity of its passive oxide layer. The α-phase typically offers better corrosion resistance due to its ability to form a more stable passive film. On the other hand, a higher proportion of β-phase grains can increase electrochemical activity, as the β-phase is generally anodic compared to the α-phase, potentially leading to galvanic corrosion [52]. Microstructures with finer grains typically contain more grain boundaries, and these can serve as locations for localized corrosion due to their higher energy and increased reactivity in these areas. However, these fine grains also tend to cause more uniform corrosion because of the consistent distribution of active sites. In contrast, coarser grains with fewer boundaries may exhibit less uniform corrosion, yet they can develop localized corrosion, particularly in regions where the β-phase is concentrated [53]. The low corrosion current density and high polarization resistance observed in the samples can be attributed to the formation of a temporary and unstable passive layer on the surface [54]. While this layer may offer sufficient protection during the short duration of the Tafel test, its instability becomes evident under prolonged electrochemical evaluation, such as electrochemical impedance spectroscopy.

Fig. 10 shows the fitted data using Nyquist, Bode, and Bode-phase plots for several samples. The data were analyzed using an equivalent circuit model (Fig. 10a) and fitted using nonlinear least squares fitting in the ZView software. The quality of the fit was assessed based on the chi-squared value to ensure an accurate depiction of the electrochemical behavior. It is commonly known that a higher arc radius indicates a higher R_{ct} and better corrosion resistance in the Nyquist plot. Chen et al. demonstrated notable electrochemical anisotropic behavior across the -X, -Y, and -Z planes of SLM samples [55]. According to the fitted data [56] from the Nyquist plot (Fig. 10b), SLM XY-x, SLM XY-y, and EBM XX-y samples, have the largest arc radius among all the specimens. This indicates that this group has the highest charge transfer resistance and the best corrosion resistance. The R_s in the proposed equivalent electrical circuit corresponds to the solution resistance, while Rct denotes the charge transfer resistance. The constant phase element (CPE) essentially replaces the ideal capacitor, and the double layer capacitance (CPEdl) is linked to the electrical double layer that forms at the interface between the Ti64 surface and the electrolyte [57]. Better corrosion resistance and lower corrosion rates are generally linked to fewer electrochemical reactions at the metal/electrolyte interface. This behavior is often reflected by a higher R_{ct}, and in systems with passive films, a higher R_f indicates a more protective surface layer. Furthermore, higher impedance at lower frequencies suggests strong resistance to ion movement and electrochemical reactions, indicating that the material's surface is well-protected [58]. In the Bode-phase plot, a higher and broader phase angle spanning the intermediate frequency range typically signifies stable capacitive behavior, which is indicative of a well-formed and protective passive layer that reflects the enhanced corrosion resistance of the sample [59]. A protective passive layer minimizes the number of active sites available for electrochemical reactions on the metal surface, thereby slowing down the corrosion process overall. When the passive layer breaks down, the low charge transfer resistance can mean that the underlying metal is more vulnerable to electron transfer, which could result in localized corrosion. The overall corrosion rate, however, stays modest as long as the passive layer is maintained (Table 4).

3.5. Density and total porosity

Achieving a completely dense product has traditionally been a key objective of additive manufacturing, as porosity remains present in conventional manufacturing methods such as casting [60]. The properties of the powder, including the size and composition of the material, as well as the manufacturing conditions, significantly impact porosity and, consequently, relative density [61,62]. The mechanical behavior of products is strongly influenced by porosity. The relative density, as determined by the Archimedes method, can be mathematically related to porosity, which is expressed as a volume percentage. The results show that the total number and volume of holes per unit volume (Table 5) in EBM samples are greater compared to those in SLM samples. The two basic forms of frequently observed pores are spherical and elongated morphologies [63]. Gaseous entrapment during solidification in the process may also result in pore formation during EBM and SLM [3].

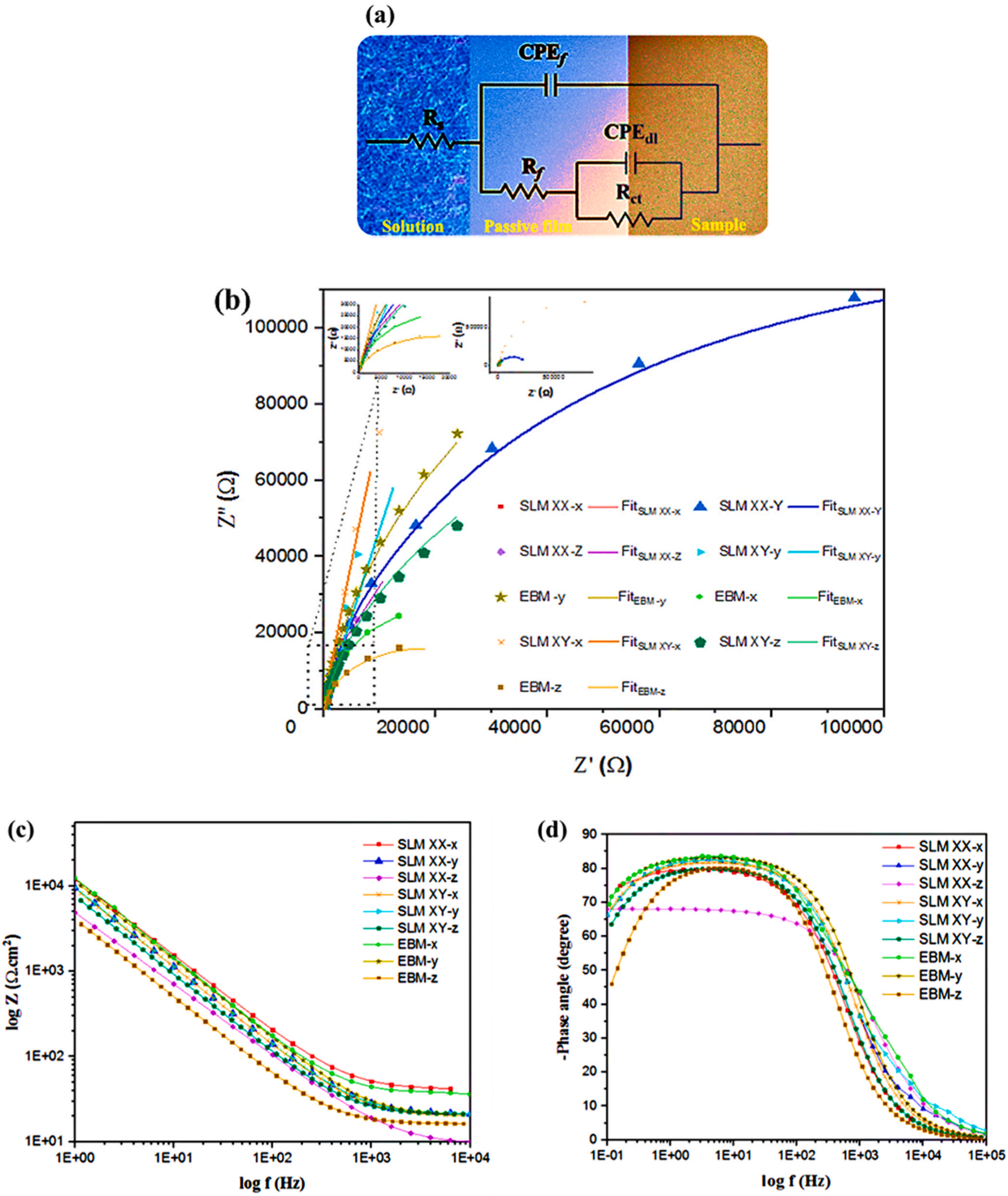

Fig. 10. (a) Equivalent electrical circuit diagram obtained using the Zview program, (b) Nyquist, (c) Bode, and (d) Bode-phase plots of the samples.

Table 4
Parameters obtained from EIS fitting of the AM Ti-6Al-4V substrates.

Sample	R_s ($\Omega.cm^2$)	$Y0_c$ ($S.sec^n.cm^{-2}$)	n_1	R_f ($\Omega.cm^2$)	$Y0_{dl}$ ($S.sec^n.cm^{-2}$)	n_2	R_{ct} ($\Omega.cm^2$)
EBM XX- (YZ)	2.83	1.12×10^{-6}	0.91	15.32	3.21×10^{-5}	0.92	2.38×10^{4}
EBM XX- (XZ)		7.65×10^{-6}	0.76	52.86	1.01×10^{-5}	0.88	1.37×10^{6}
	4.44						
EBM XX- (XY)	2.62	4.12×10^{-6}	0.86	13.44	8.91×10^{-6}	0.92	1.27×10^{4}
SLM XX- (YZ)	4.84	1.91×10^{-5}	0.94	21.02	1.91×10^{-5}	0.92	2.55×10^{5}
SLM XX- (XZ)	2.38	1.01×10^{-6}	0.92	19.55	3.65×10^{-5}	0.94	7.36×10^{4}
SLM XX- (XY)	2.93	1.38×10^{-6}	0.92	18.65	3.75×10^{-5}	0.93	7.51×10^{4}
SLM XY- (YZ)	4.07	9.49×10^{-7}	0.85	71.02	1.05×10^{-5}	0.89	4.45×10^{6}
SLM XY- (XZ)	4.19	1.54×10^{-6}	0.81	43.49	1.38×10^{-5}	0.91	6.07×10^{5}
SLM XY- (XY)	2.95	1.73×10^{-6}	0.88	16.78	3.38×10^{-5}	0.92	6.54×10^{4}

Table 5
The relevant density and porosity of samples fabricated by AM process.

Ti6Al4V	ρ_{bulk}	Porosity (%)
SLM- XX	4.28	3.4 %
SLM- XY	4.31	2.8 %
EBM- XX	4.17	5.9 %

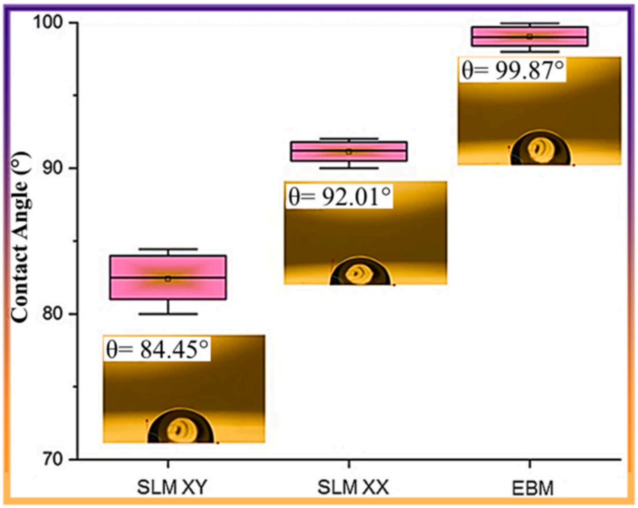

Fig. 11. Contact angle measurements for the (a) SLM-XY, (b) SLM-XX, and (c) EBM-XX samples.

Upon cooling, the alloy vapour may be retained and condense into nearly spherical pores. Insufficient melting during subsequent layer deposition causes the elongated pores [64,65]. As presented in Table 5, the density trend can be correlated with laser energy density. SLM-XY used the highest energy density during fabrication and achieved the highest densification, while EBM, with the lowest energy density, exhibited the lowest densification.

3.6. *Surface wettability*

Fig. 11 displays the wettability characteristics of the Ti64 alloys. The EBM samples exhibited the highest water contact angle of 99.87°, while the SLM-XY Ti64 alloy showed the lowest water contact angle of 84.45°. Hydrophobicity and the alloy's surface energy are closely related, with more hydrophobic properties resulting in surfaces with higher water contact angles. A surface is considered hydrophilic when the contact angle between the surface and a water droplet is below 90°, while it is regarded as hydrophobic if the contact angle exceeds 90° [66]. The performance of biomaterials is affected by the hydrophilic/hydrophobic characteristics of their surfaces. SLM approaches reveal that altering the scan strategy significantly affects the hydrophobicity of the surfaces [67]. This can be attributed to the interaction between the laser direction and the argon airflow direction, which might result in irregularities in microstructural features. For instance, unmelted regions are linked to inadequate energy density during the scanning process, which can occur due to improper scanning parameters (such as current, scanning speed, focus offset, line offset, etc.) or the influence of electromagnetic interference during fabrication. Electromagnetic interference in the melt pool during additive manufacturing arises from the interaction of electric and magnetic fields with the molten material. This interference can destabilize the melt pool and alter its dynamics, potentially resulting in defects in the final part. These regions can create surface irregularities, such as pores or rough spots, which can impact the wettability of the material [68].

3.7. *Microhardness and surface roughness*

Fig. 12 summarizes the microhardness and roughness characteristics of the Ti64 samples. The SLM and EBM fabrication methods produce different microhardness values due to distinctions in their microstructures. Ti64 alloys produced through laser techniques consist of acicular α′ martensite, whereas EBM-manufactured components exhibit an α+ β microstructure. Among these microstructures, α′ martensite demonstrates the highest strength [69]. It is a non-equilibrium phase, stronger than the α+ β phases due to lattice strains that develop during its formation. Furthermore, columnar α+ β microstructures exhibit better strength than equiaxed α+ β microstructures. Overall, characteristic altered α/β structures, including colony and basket-weave morphologies, are observed in the EBM-built samples [70]. It is well known that the acicular α′ phase results in higher hardness than the α/β microstructure. Moreover, an increase in oxygen contamination leads to a thicker oxide coating with higher surface hardness, and the surface colour shifts from silver to a deeper blue [71,72]. The microhardness of three different samples (SLM-XX, SLM-XY, and EBM-XX) was found to be

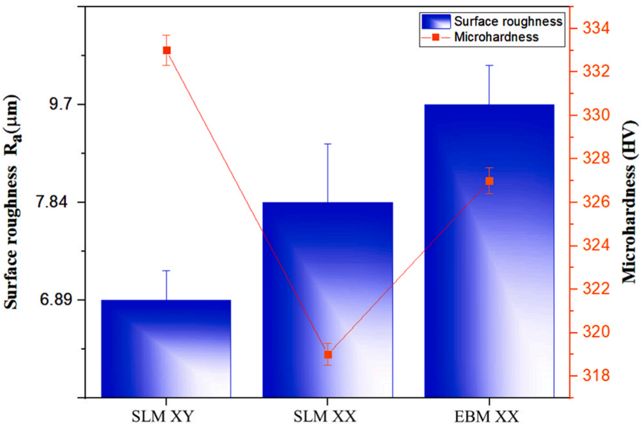

Fig. 12. Microhardness and surface roughness of the (a) SLM-XY, (b) SLM-XX, and (c) EBM-XX samples.

319.5, 333.66, and 327.66 HV, respectively. The variation in microhardness between the SLM-XX and SLM-XY orientations can be attributed to the anisotropic effects inherent in the SLM process. SLM fabricates components layer by layer, resulting in anisotropic material properties that depend on the scanning direction. Moreover, the grain size and orientation in the SLM-XY sample are typically more refined and structured, enhancing hardness due to the rapid cooling and solidification occurring along the laser's scanning path. In contrast, grains in the SLM-XX sample tend to grow larger or adopt different orientations due to slower cooling rates and heat retention across multiple layers, leading to reduced hardness [73]. Furthermore, the differing cooling rates between the SLM-XY and SLM-XX samples can create variations in the residual stresses that affect microhardness. The SLM-XX sample also exhibits more defects, such as porosity and incomplete melting, which can further diminish hardness compared to the SLM-XY, where the laser scanning process is more uniform [74].

The cooling rates and solidification patterns can vary in different directions during the SLM and EBM processes, leading to the observed differences in grain size and shape [75,76]. EBM operates at higher temperatures and utilizes an electron beam, resulting in slower cooling rates. This slower cooling leads to the formation of coarser microstructures, which may exhibit lower hardness [77]. SLM typically has lower porosity than EBM, reducing defect density and enhancing effective hardness, as defects can serve as stress concentrators that diminish overall mechanical performance [78]. In the SLM-XY sample, the laser operates in the XY plane, resulting in more consistent heat distribution and a finer microstructure (harder phases) in that orientation. On the other hand, elevated temperatures in EBM can enhance phase stability and reduce the formation of residual stresses, leading to increased hardness [79]. Conversely, residual stresses in components processed by SLM-XX differ from those in EBM parts due to their distinct thermal cycles. These variations in thermal cycles and solidification processes can result in variations in the phase composition of materials created by SLM and EBM [80,81]. On the other hand, EBM operates at higher temperatures, which can result in a more isotropic microstructure and contribute to higher overall hardness compared to SLM-XX [82]. The surfaces of the SLM (XX, XY) and EBM-XX samples were rough, with values of 7.84 ± 0.4, 6.89 ± 0.34, and 9.7 ± 0.6 μm, respectively. In contrast to the other samples, the surface of the SLM-XY was the smoothest, while the surfaces of the EBM samples were considerably rougher. EBM appears to produce a broader molten pool, which hinders the formation of a smooth surface [83,84]. For the SLM samples, the effect of orientation was found to increase the roughness of the XX surfaces. In general, the staircase effect due to more layers, the adherence of partially melted granules to the outer surface, and the presence of unmelted areas and open pores are among the factors that cause surface roughness. Ponader et al. [85] suggested that Ti64 samples with a surface roughness of less than 24.9 μm are suitable for cell growth. Conversely, a surface roughness greater than 56.9 μm was found to decrease the proliferation of human osteoblast cells. According to previous studies [86], different process orientations altered the surface roughness and enhanced the "valley and hill" effects on the surfaces.

3.8. *Evaluation of bioactivity*

Simulated body fluid was employed in this study to assess the bioactivity of the samples. The process involved immersing the samples for 21 days in a 1X SBF solution (pH = 7.4), which mimics the characteristics of human plasma, to monitor the production of calcium phosphate crystals on AM samples after initial etching. During the etching step, the metal surfaces were treated with an acid solution not only for cleaning but also to modify their roughness. Acid-etched surfaces, particularly in titanium, exhibit enhanced adhesion and improved roughness [66]. The 1X SBF is created in the lab with ionic concentrations that closely match those found in blood plasma [87]. Fig. 13 shows SEM images of the AM samples after 21 days of immersion in 1X SBF solution, revealing calcium phosphate precipitation on all sample surfaces. However, the precipitation of calcium phosphate on the surface of the Ti64 samples differed depending on the additive manufacturing process. Calcium phosphate crystals grew more on the SLM samples (Fig. 13a and c) compared to the EBM sample (Fig. 13b). This result can primarily be correlated with the differences in surface roughness and contact angle [88,89]. Surface roughness can enhance calcium phosphate deposition by providing additional surface area and micro-scale features that serve as nucleation sites for crystals. Rough surfaces typically result in greater calcium phosphate accumulation, as they promote stronger mechanical bonding and better adhesion of the calcium phosphate layer [90]. Most SLM samples show calcium phosphate accumulation in the form of islands. Fig. 14(a), (b), and (c) display the EDS results for the SLM-XY, EBM-XX, and SLM-XX samples, respectively. The SLM-XY surface has a higher Ca^{2+} concentration in the calcium phosphate layer than the SLM-XX surface, which correlates with a lower contact angle. This further demonstrates that altering the production process facilitates the development of surface calcium phosphate layers. On the other hand, the EBM XX samples, due to their higher contact angle, contain less Ca and P than the SLM samples, resulting in decreased calcium phosphate accumulation.

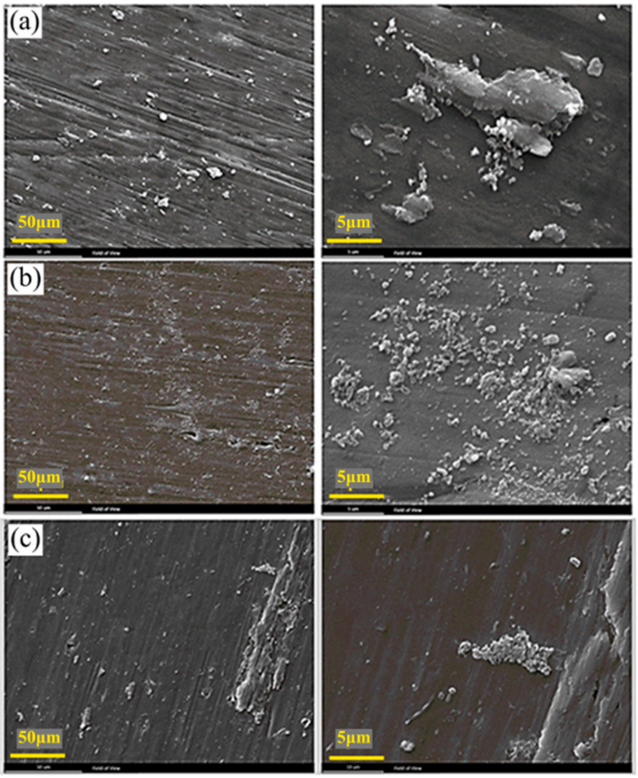

Fig. 13. Surface morphology of the (a) SLM XY, (b) EBM XX, and (c) SLM XX samples after soaking in SBF for 21 days.

4. Conclusion

In this study, Ti64 components were fabricated using both SLM and EBM techniques. The results indicate several key findings:

- Phase Composition and Microstructure: SEM and XRD analyses revealed that the manufacturing method significantly influenced the chemical composition and microstructure of the components.
- Microhardness and Roughness: SLM XY-processed samples exhibited higher microhardness compared to EBM samples. Conversely, SLM samples had lower surface roughness than those processed by EBM.

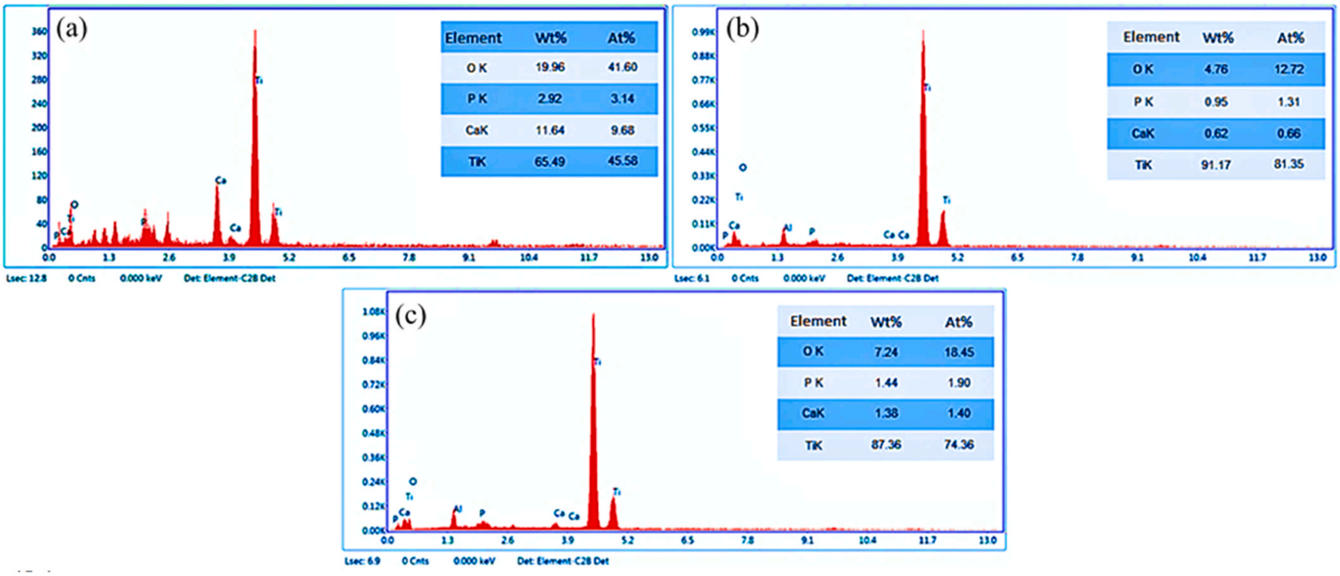

(a)

Element	Wt%	At%
O K	19.96	41.60
P K	2.92	3.14
CaK	11.64	9.68
TiK	65.49	45.58

(b)

Element	Wt%	At%
O K	4.76	12.72
P K	0.95	1.31
CaK	0.62	0.66
TiK	91.17	81.35

(c)

Element	Wt%	At%
O K	7.24	18.45
P K	1.44	1.90
CaK	1.38	1.40
TiK	87.36	74.36

Fig. 14. EDS spectrum of (a) SLM XY, (b) EBM XX, and (c) SLM XX samples after the soaking in SBF.

- Electrochemical Properties: All as-fabricated samples (SLM XX, XY, and EBM YZ-plane, XZ-plane, XY-plane) demonstrated good electrochemical properties. However, electrochemical polarization Tafel curves and impedance data consistently showed that XY-plane samples had lower corrosion resistance than those in the XZ-plane and YZ-plane.
- Bioactivity: In vitro assays revealed that SLM XY samples exhibited high bioactivity, with more calcium phosphate deposits on their surfaces, which correlated with wettability properties.

Therefore, both EBM and SLM (XX, XY) Ti64 components are promising candidates for orthopedic biomaterials. Future research will focus on coating the samples to improve the distribution of hydroxyapatite elements (Ca/P), achieve a bone-like molar ratio, enhance bone cell functions, and improve antibacterial properties.

CRediT authorship contribution statement

Masoud Atapour: Writing – review & editing, Visualization, Supervision, Resources. **Ozkan Gokcekaya:** Writing – review & editing, Project administration, Methodology, Investigation, Conceptualization. **Parinaz Mofazali:** Writing – original draft, Visualization, Software, Methodology, Investigation, Formal analysis, Data curation, Conceptualization. **Batur Ercan:** Writing – review & editing, Investigation, Conceptualization. **Takayoshi Nakano:** Project administration, Funding acquisition. **Sung-Hyun Park:** Writing – review & editing, Investigation.

Declaration of Competing Interest

The authors declare that they have no known competing financial interests or personal relationships that could have appeared to influence the work reported in this paper.

Acknowledgements

We appreciate the support from the Centre for International Scientific Studies and Collaboration CISSC (Iran) and Scientific and Technological Research Council of Türkiye (TÜBİTAK) within the framework of the Shams Tabrizi Call MSRT-TUBITAK Joint Research Program.

Data availability

Data will be made available on request.

References

[1] P. Mofazali, M. Atapour, M. Nakamura, M. Galati, A. Saboori, Evaluation of layer-by-layer assembly systems for drug delivery and antimicrobial properties in orthopaedic application, Int. J. Pharm. 657 (2024) 124148, https://doi.org/10.1016/j.ijpharm.2024.124148.

[2] Z. Eren, O. Gokcekaya, D. Balkan, T. Nakano, Z. Mecitoğlu, Comparison of in-plane compression of additively manufactured Ti6Al4V 2D auxetic structures: lattice design, manufacturing speed, and failure mode, Mater. Des. 241 (2024) 112885, https://doi.org/10.1016/j.matdes.2024.112885.

[3] J.C. Vasco, Additive manufacturing for the automotive industry. in: Addit. Manuf, Elsevier, 2021, pp. 505–530.

[4] A. Pajonk, A. Prieto, U. Blum, U. Knaack, Multi-material additive manufacturing in architecture and construction: a review, J. Build. Eng. 45 (2022) 103603.

[5] I. Buj-Corral, A. Tejo-Otero, F. Fenollosa-Artés, Development of AM technologies for metals in the sector of medical implants, Metals 10 (2020), https://doi.org/10.3390/met10050686.

[6] T. Pereira, J.V. Kennedy, J. Potgieter, A comparison of traditional manufacturing vs additive manufacturing, the best method for the job, Procedia Manuf. 30 (2019) 11–18, https://doi.org/10.1016/j.promfg.2019.02.003.

[7] J. Corona-Castuera, D. Rodriguez-Delgado, J. Henao, J.C. Castro-Sandoval, C. A. Poblano-Salas, Design and fabrication of a customized partial hip prosthesis employing CT-scan data and lattice porous structures, ACS Omega 6 (2021) 6902–6913, https://doi.org/10.1021/acsomega.0c06144.

[8] O. Gokcekaya, T. Ishimoto, Y. Nishikawa, Y.S. Kim, A. Matsugaki, R. Ozasa, M. Weinmann, C. Schnitter, M. Stenzel, H.S. Kim, Novel single crystalline-like non-equiatomic TiZrHfNbTaMo bio-high entropy alloy (BioHEA) developed by laser powder bed fusion, Mater. Res. Lett. 11 (2023) 274–280.

[9] C. Culmone, G. Smit, P. Breedveld, Additive manufacturing of medical instruments: a state-of-the-art review, Addit. Manuf. 27 (2019) 461–473.

[10] M. Pérez, D. Carou, E.M. Rubio, R. Teti, Current advances in additive manufacturing, Procedia CIRP 88 (2020) 439–444, https://doi.org/10.1016/j.procir.2020.05.076.

[11] S.L. Sing, J. An, W.Y. Yeong, F.E. Wiria, Laser and electron-beam powder-bed additive manufacturing of metallic implants: a review on processes, materials and designs, J. Orthop. Res. 34 (2016) 369–385.

[12] P. Badoniya, M. Srivastava, P.K. Jain, S. Rathee, A state-of-the-art review on metal additive manufacturing: milestones, trends, challenges and perspectives, J. Braz. Soc. Mech. Sci. Eng. 46 (2024) 339, https://doi.org/10.1007/s40430-024-04917-8.

[13] K. Maji, K. Pramanik, Additive Manufacturing of Orthopaedic Implants. in: Adv. 3D Bioprinting, CRC Press, 2024, pp. 173–193.

[14] A.M. Nyakundi, M.R. Maina, R.V.S. Prasad, E.O. Olakanmi, S. Pityana, Optimization of functional performance of additively manufactured cobalt-chromium-molybdenum alloy for dental implant applications, J. Manuf. Process 120 (2024) 1087–1103, https://doi.org/10.1016/j.jmapro.2024.05.005.

[15] J.A. Tamayo, M. Riascos, C.A. Vargas, L.M. Baena, Additive manufacturing of Ti6Al4V alloy via electron beam melting for the development of implants for the biomedical industry, Heliyon 7 (2021).

[16] Q. Zhang, Y. Guan, Application of metal additive manufacturing in oral dentistry, Curr. Opin. Biomed. Eng. 25 (2023) 100441.

[17] P. Mofazali, M. Atapour, M. Nakamura, M. Sheikholeslam, M. Galati, A. Saboori, Surface modification of additive manufactured Ti6Al4V scaffolds with gelatin/alginate- IGF-1 carrier: an effective approach for healing bone defects, Int. J. Biol. Macromol. (2024) 131125, https://doi.org/10.1016/j.ijbiomac.2024.131125.

[18] L. Romero Reséndiz, T. Sánchez Cano, M. Naeem, A. Ur Rehman, E. Salamci, V. Torres Mendoza, E. Degalez Duran, L. Bazán Díaz, M.U. Salamci, Mechanical and electrochemical properties comparison of additively manufactured Ti-6Al-4V alloys by electron beam melting and selective laser melting, J. Mater. Eng. Perform. (2024) 1–11.

[19] D. Santonocito, S. Fintová, V. Di Cocco, F. Iacoviello, G. Risitano, D. D'Andrea, Comparison on mechanical behavior and microstructural features between traditional and AM AISI 316L, Fatigue Fract. Eng. Mater. Struct. 46 (2023) 379–395.

[20] Y. Liu, Z. Shan, X. Yang, H. Jiao, W. Huang, Effect of scanning strategies on the microstructure and mechanical properties of Ti-22Al-25Nb alloy fabricated through selective laser melting, Metals 13 (2023), https://doi.org/10.3390/met13030634.

[21] J. Chen, Z. Liu, C. Liu, B. Zhang, T. Liu, G. Chen, M. Qin, X. Qu, Effects of scanning strategy and scanning speed on microstructures and mechanical properties of NiTi alloys by laser powder bed fusion, Mater. Sci. Eng. A. 914 (2024) 147115, https://doi.org/10.1016/j.msea.2024.147115.

[22] S.-H. Park, O. Gokcekaya, T. Nitomakida, T. Nakano, Effects of heat accumulation strategies on defects and microstructure of pure chromium fabricated by laser powder bed fusion: an experimental and numerical study, J. Mater. Res. Technol. 33 (2024) 7333–7344, https://doi.org/10.1016/j.jmrt.2024.11.049.

[23] A. Sharma, M.C. Oh, J.-T. Kim, A.K. Srivastava, B. Ahn, Investigation of electrochemical corrosion behavior of additive manufactured Ti–6Al–4V alloy for medical implants in different electrolytes, J. Alloy. Compd. 830 (2020) 154620, https://doi.org/10.1016/j.jallcom.2020.154620.

[24] D.-C. Serbanoiu, A.-C. Vartolomei, D.-V. Ghiga, S.I. Pop, I. Panainte, M. Moldovan, C. Sarosi, I. Petean, M.-J. Boileau, M. Pacurar, Comparative evaluation of dental enamel microhardness following various methods of interproximal reduction: a Vickers hardness tester investigation, Biomedicines 12 (2024), https://doi.org/10.3390/biomedicines12051132.

[25] T. Kokubo, H. Kushitani, S. Sakka, T. Kitsugi, T. Yamamuro, Solutions able to reproduce in vivo surface-structure changes in bioactive glass-ceramic A-W3, J. Biomed. Mater. Res. 24 (1990) 721–734.

[26] A.A. Al-Tamimi, M.A. Hernandez, A. Omar, D.F. Morales-Aldana, C. Peach, P. Bartolo, Mechanical, biological and tribological behaviour of fixation plates 3D printed by electron beam and selective laser melting, Int. J. Adv. Manuf. Technol. 109 (2020) 673–688, https://doi.org/10.1007/s00170-020-05676-1.

[27] B. Wysocki, P. Maj, R. Sitek, J. Buhagiar, K.J. Kurzydłowski, W. Święszkowski, Laser and electron beam additive manufacturing methods of fabricating titanium bone implants, Appl. Sci. 7 (2017), https://doi.org/10.3390/app7070657.

[28] M. Zhang, Y. Yang, D. Wang, Z. Xiao, C. Song, C. Weng, Effect of heat treatment on the microstructure and mechanical properties of Ti6Al4V gradient structures manufactured by selective laser melting, Mater. Sci. Eng. A. 736 (2018) 288–297, https://doi.org/10.1016/j.msea.2018.08.084.

[29] H. Yu, F. Li, Z. Wang, X. Zeng, Fatigue performances of selective laser melted Ti-6Al-4V alloy: influence of surface finishing, hot isostatic pressing and heat treatments, Int. J. Fatigue 120 (2019) 175–183.

[30] B. Vrancken, L. Thijs, J.-P. Kruth, J. Van Humbeeck, Heat treatment of Ti6Al4V produced by selective laser melting: microstructure and mechanical properties, J. Alloy. Compd. 541 (2012) 177–185, https://doi.org/10.1016/j.jallcom.2012.07.022.

[31] S.Q. Wu, Y.J. Lu, Y.L. Gan, T.T. Huang, C.Q. Zhao, J.J. Lin, S. Guo, J.X. Lin, Microstructural evolution and microhardness of a selective-laser-melted Ti–6Al–4V alloy after post heat treatments, J. Alloy. Compd. 672 (2016) 643–652.

[32] N. Eshawish, S. Malinov, W. Sha, P. Walls, Microstructure and mechanical properties of Ti-6Al-4V manufactured by selective laser melting after stress relieving, hot isostatic pressing treatment, and post-heat treatment, J. Mater. Eng. Perform. 30 (2021) 5290–5296, https://doi.org/10.1007/s11665-021-05753-w.

[33] S.-H. Park, O. Gokcekaya, M.-H. Oh, T. Nakano, Effects of hatch spacing on densification, microstructural and mechanical properties of β-solidifying γ-TiAl alloy fabricated by laser powder bed fusion, Mater. Charact. 214 (2024) 114077, https://doi.org/10.1016/j.matchar.2024.114077.

[34] W. Xiang, W. Yuan, H. Deng, H. Luo, L. Chen, W. Yin, Effect of aging temperature on the microstructure and mechanical properties of a novel β titanium alloy, Materials 16 (2023) 7393.

[35] R.R. Kamath, P. Nandwana, Y. Ren, H. Choo, Solidification texture, variant selection, and phase fraction in a spot-melt electron-beam powder bed fusion processed Ti-6Al-4V, Addit. Manuf. 46 (2021) 102136, https://doi.org/10.1016/j.addma.2021.102136.

[36] R. Jindal, Effect of grain refinement on corrosion resistance, Int. Res. J. Eng. Technol. (IRJET) 7 (2020) 343–346.

[37] A. Sotniczuk, B. Dou, C. Xie, J. Tang, D. Kalita, W. Chromiński, H. Garbacz, F. Sun, K. Ogle, New insights into the corrosion of orthopedic Ti-6Al-4V under cathodic polarization, Corros. Sci. (2024) 112354.

[38] M. Hoseini, A. Shahryari, S. Omanovic, J.A. Szpunar, Comparative effect of grain size and texture on the corrosion behaviour of commercially pure titanium processed by equal channel angular pressing, Corros. Sci. 51 (2009) 3064–3067.

[39] V. Singh, C. Mondal, A. Kumar, P.P. Bhattacharjee, P. Ghosal, High temperature compressive flow behavior and associated microstructural development in a β-stabilized high Nb-containing γ-TiAl based alloy, J. Alloy. Compd. 788 (2019) 573–585, https://doi.org/10.1016/j.jallcom.2019.02.207.

[40] H. Amano, T. Ishimoto, K. Hagihara, R. Suganuma, K. Aiba, S.-H. Sun, P. Wang, T. Nakano, Impact of gas flow direction on the crystallographic texture evolution in laser beam powder bed fusion, Virtual Phys. Prototyp. 18 (2023) e2169172, https://doi.org/10.1080/17452759.2023.2169172.

[41] S.I. Wright, M.M. Nowell, D.P. Field, A review of strain analysis using electron backscatter diffraction, Microsc. Microanal. Off. J. Microsc. Soc. Am. Microbe Anal. Soc. Microsc. Soc. Can. 17 (2011) 316–329, https://doi.org/10.1017/S1431927611000055.

[42] R. Ullah, J. Lu, L. Sang, M. Rizwan, Y. Zhang, Z. Zhang, Investigating the microstructural evolution during deformation of laser additive manufactured Ti–6Al–4V at 400 °C using in-situ EBSD, Mater. Sci. Eng. A. 823 (2021) 141761, https://doi.org/10.1016/j.msea.2021.141761.

[43] Y. Luo, Y. Deng, L. Guan, L. Ye, X. Guo, A. Luo, Effect of grain size and crystal orientation on the corrosion behavior of as-extruded Mg-6Gd-2Y-0.2Zr alloy, Corros. Sci. 164 (2020) 108338, https://doi.org/10.1016/j.corsci.2019.108338.

[44] N. Birbilis, K.D. Ralston, S. Virtanen, H.L. Fraser, C.H.J. Davies, Grain character influences on corrosion of ECAPed pure magnesium, Corros. Eng. Sci. Technol. 45 (2010) 224–230, https://doi.org/10.1179/147842209X12559428167805.

[45] C. de Formanoir, S. Michotte, O. Rigo, L. Germain, S. Godet, Electron beam melted Ti–6Al–4V: microstructure, texture and mechanical behavior of the as-built and heat-treated material, Mater. Sci. Eng. A. 652 (2016) 105–119.

[46] K.K. Alaneme, E.A. Okotete, Recrystallization mechanisms and microstructure development in emerging metallic materials: a review, J. Sci. Adv. Mater. Devices 4 (2019) 19–33, https://doi.org/10.1016/j.jsamd.2018.12.007.

[47] L. Zhou, H. Liu, C. Yan, Y. Wei, Z. Xia, H. Peng, J. Tang, Electrochemical behavior of laser powder bed fusion (L-PBF) Ti–6Al–4V alloy: influence of phase and grain boundaries on surface passive film formation, Met. Mater. Int. (2024) 1–14.

[48] W.D. Callister, D.G. Rethwisch, Materials science and engineering: an introduction, Wiley New York, 1999.

[49] H. Tekdir, T. Yetim, A.F. Yetim, Corrosion properties of ceramic-based TiO2 films on plasma oxidized Ti6Al4V/316l layered implant structured manufactured by selective laser melting, J. Bionic Eng. 18 (2021) 944–957, https://doi.org/10.1007/s42235-021-0055-6.

[50] N. Dai, L.-C. Zhang, J. Zhang, X. Zhang, Q. Ni, Y. Chen, M. Wu, C. Yang, Distinction in corrosion resistance of selective laser melted Ti-6Al-4V alloy on different planes, Corros. Sci. 111 (2016) 703–710, https://doi.org/10.1016/j.corsci.2016.06.009.

[51] Y. Xiao, N. Dai, Y. Chen, J. Zhang, S.-W. Choi, On the microstructure and corrosion behaviors of selective laser melted CP-Ti and Ti-6Al-4V alloy in Hank's artificial body fluid, Mater. Res. Express 6 (2019) 126521.

[52] V. Dehnavi, J.D. Henderson, C. Dharmendra, B.S. Amirkhiz, D.W. Shoesmith, J. J. Noël, M. Mohammadi, Corrosion behaviour of electron beam melted Ti6Al4V: effects of microstructural variation, J. Electrochem. Soc. 167 (2020) 131505.

[53] S. Usha Rani, V.V. Anusha Thampi, D. Kesavan, S. Ramanathan, M. Kamaraj, An integrated investigation of the effect of sub-transus treatment on the microstructure and corrosion behaviour of the LPBF Ti–6Al–4V alloy, Mater. Chem. Phys. 322 (2024) 129555, https://doi.org/10.1016/j.matchemphys.2024.129555.

[54] P. Bocchetta, L.-Y. Chen, J.D.C. Tardelli, A.C. dos Reis, F. Almeraya-Calderón, P. Leo, Passive layers and corrosion resistance of biomedical Ti-6Al-4V and β-Ti alloys, Coatings 11 (2021) 487.

[55] L.Y. Chen, J.C. Huang, C.H. Lin, C.T. Pan, S.Y. Chen, T.L. Yang, D.Y. Lin, H.K. Lin, J.S.C. Jang, Anisotropic response of Ti-6Al-4V alloy fabricated by 3D printing selective laser melting, Mater. Sci. Eng. A 682 (2017) 389–395, https://doi.org/10.1016/j.msea.2016.11.061.

[56] J. Huang, W. Zhang, H. Xu, W. Fang, Effect of heat treatment on corrosion properties of Ti-6Al-4V titanium alloy produced by electron powder bed fusion, JOM 76 (2024) 3039–3049, https://doi.org/10.1007/s11837-024-06537-y.

[57] X. Liu, S. Chen, J. Zhang, G. Yang, Y. Zhang, T. Wang, J. Lei, Enhancement of the electrochemical corrosion resistance of Ti6Al4V alloy reinforced by nano-and micro-TiC particles through directed energy deposition, Corros. Sci. 221 (2023) 111343.

[58] Z. Zhao, Y. Guo, W. Du, P. Bai, Z. Zhang, L. Wang, K. Ma, S. Zhang, X. Han, C. Yang, Corrosion behavior of SiC/Ti6Al4V titanium matrix composites fabricated by SLM, J. Mater. Res. Technol. 31 (2024) 534–542, https://doi.org/10.1016/j.jmrt.2024.06.093.

[59] S. Zhou, Y. Zhao, X. Wang, W. Li, D. Chen, T.B. Sercombe, Enhanced corrosion resistance of Ti-5 wt% TiN composite compared to commercial pure Ti produced by selective laser melting in HCl solution, J. Alloy. Compd. 820 (2020) 153422, https://doi.org/10.1016/j.jallcom.2019.153422.

[60] P. Li, P.D. Lee, T.C. Lindley, D.M. Maijer, G.R. Davis, J.C. Elliott, X-ray microtomographic characterisation of porosity and its influence on fatigue crack growth, Adv. Eng. Mater. 8 (2006) 476–479.

[61] H. Wang, Effect of Processing Parameters on the Defects, Microstructure, and Property Evaluation of Ti-6Al-4V Titanium Alloy Processed by Laser Powder Bed Fusion, (2024). https://doi.org/10.1063/7.0001251.

[62] S. Cao, Y. Zou, C.V.S. Lim, X. Wu, Review of laser powder bed fusion (LPBF) fabricated Ti-6Al-4V: process, post-process treatment, microstructure, and property, Light Adv. Manuf. 2 (n.d.) 313–332. https://doi.org/10.37188/lam.2021.020.

[63] M. Wang, H.Q. Li, D.J. Lou, C.X. Qin, J. Jiang, X.Y. Fang, Y.B. Guo, Microstructure anisotropy and its implication in mechanical properties of biomedical titanium alloy processed by electron beam melting, Mater. Sci. Eng. A 743 (2019) 123–137, https://doi.org/10.1016/j.msea.2018.11.038.

[64] K. Darvish, Z.W. Chen, T. Pasang, Reducing lack of fusion during selective laser melting of CoCrMo alloy: effect of laser power on geometrical features of tracks, Mater. Des. 112 (2016) 357–366, https://doi.org/10.1016/j.matdes.2016.09.086.

[65] T. Mukherjee, J.S. Zuback, A. De, T. DebRoy, Printability of alloys for additive manufacturing, Sci. Rep. 6 (2016) 19717, https://doi.org/10.1038/srep19717.

[66] G. Wen, Y. Zhang, S. Xie, W. Dong, The influence of two distinct surface modification techniques on the clinical efficacy of titanium implants: a systematic review and meta-analysis, J. Stomatol. Oral. Maxillofac. Surg. (2024) 101855, https://doi.org/10.1016/j.jormas.2024.101855.

[67] I. Gibson, D.W. Rosen, B. Stucker, M. Khorasani, D. Rosen, B. Stucker, M. Khorasani, Additive manufacturing technologies, Springer, 2021.

[68] T. DebRoy, H.L. Wei, J.S. Zuback, T. Mukherjee, J.W. Elmer, J.O. Milewski, A. M. Beese, A. de Wilson-Heid, A. De, W. Zhang, Additive manufacturing of metallic components–process, structure and properties, Prog. Mater. Sci. 92 (2018) 112–224.

[69] J. Yang, H. Yu, J. Yin, M. Gao, Z. Wang, X. Zeng, Formation and control of martensite in Ti-6Al-4V alloy produced by selective laser melting, Mater. Des. 108 (2016) 308–318.

[70] M. Yuan, X. Zhao, Q. Yue, Y. Gu, Z. Zhang, The effect of microstructure on the very high cycle fatigue behavior of Ti-6Al-4V alloy, Metals 14 (2024), https://doi.org/10.3390/met14030254.

[71] Y. Takayama, R. Nomoto, H. Nakajima, C. Ohkubo, Effects of argon gas flow rate on laser-welding, Dent. Mater. J. 31 (2012) 316–326.

[72] B.E. Carroll, T.A. Palmer, A.M. Beese, Anisotropic tensile behavior of Ti–6Al–4V components fabricated with directed energy deposition additive manufacturing, Acta Mater. 87 (2015) 309–320, https://doi.org/10.1016/j.actamat.2014.12.054.

[73] J. Yang, H. Yu, Z. Wang, X. Zeng, Effect of crystallographic orientation on mechanical anisotropy of selective laser melted Ti-6Al-4V alloy, Mater. Charact. 127 (2017) 137–145.

[74] H. Ali, H. Ghadbeigi, K. Mumtaz, Processing parameter effects on residual stress and mechanical properties of selective laser melted Ti6Al4V, J. Mater. Eng. Perform. 27 (2018) 4059–4068.

[75] D. June, J.R. Mayeur, P. Gradl, A. Wessman, K. Hazeli, Effects of size, geometry, and testing temperature on additively manufactured Ti-6Al-4V titanium alloy, Addit. Manuf. 80 (2024) 103970.

[76] J. Yin, G. Peng, C. Chen, J. Yang, H. Zhu, L. Ke, Z. Wang, D. Wang, M. Ma, G. Wang, Thermal behavior and grain growth orientation during selective laser melting of Ti-6Al-4V alloy, J. Mater. Process. Technol. 260 (2018) 57–65.

[77] R. Alaghmandfard, F. Forooghi, P. Seraj, M. Keshavarzan, D. Chalasani, F. Fazeli, N. Ofori-Opoku, M. Mohammadi, Heat Treatment, Microstructure, Texture, and Mechanical Properties of Electron Beam Melted Ti6al4v, Microstruct. Texture, Mech. Prop. Electron Beam Melted Ti6al4v. (n.d.).

[78] L.P. Mocanu, C. Bellini, F. Berto, V. Di Cocco, F. Iacoviello, N. Razavi, Defects in additive manufacturing and their influence on structural integrity. in: Fatigue Addit. Manuf. Met., Elsevier, 2024, pp. 181–213.

[79] J.L. Bartlett, X. Li, An overview of residual stresses in metal powder bed fusion, Addit. Manuf. 27 (2019) 131–149, https://doi.org/10.1016/j.addma.2019.02.020.

[80] A. Takase, T. Ishimoto, N. Morita, N. Ikeo, T. Nakano, Comparison of phase characteristics and residual stresses in Ti-6Al-4V alloy manufactured by laser powder bed fusion (L-PBF) and electron beam powder bed fusion (EB-PBF) techniques, Crystals 11 (2021) 796.

[81] Y. Liu, Y. Yang, D. Wang, A study on the residual stress during selective laser melting (SLM) of metallic powder, Int. J. Adv. Manuf. Technol. 87 (2016) 647–656, https://doi.org/10.1007/s00170-016-8466-y.

[82] A. Mohammadi, B. Niroumand, A. Saboori, Microstructure, hardness and surface roughness characterization of EBM fabricated Ti-6Al-4V samples, J. Adv. Mater. Eng. 40 (2022) 51–67, https://doi.org/10.47176/jame.40.4.03322.

[83] M. Fousová, D. Vojtěch, K. Doubrava, M. Daniel, C.-F. Lin, Influence of inherent surface and internal defects on mechanical properties of additively manufactured Ti6Al4V alloy: comparison between selective laser melting and electron beam melting, Materials 11 (2018), https://doi.org/10.3390/ma11040537.

[84] F. Bartolomeu, M. Gasik, F.S. Silva, G. Miranda, Mechanical properties of Ti6Al4V fabricated by laser powder bed fusion: a review focused on the processing and microstructural parameters influence on the final properties, Metals 12 (2022), https://doi.org/10.3390/met12060986.

[85] S. Ponader, E. Vairaktaris, P. Heinl, C.V. Wilmowsky, A. Rottmair, C. Körner, R. F. Singer, S. Holst, K.A. Schlegel, F.W. Neukam, E. Nkenke, Effects of topographical surface modifications of electron beam melted Ti-6Al-4V titanium on human fetal osteoblasts, J. Biomed. Mater. Res. A 84 (2008) 1111–1119, https://doi.org/10.1002/jbm.a.31540.

[86] S.J. Foster, K. Carver, R.B. Dinwiddie, F. List, K.A. Unocic, A. Chaudhary, S.S. Babu, Process-defect-structure-property correlations during laser powder bed fusion of alloy 718: role of in situ and ex situ characterizations, Metall. Mater. Trans. A. 49 (2018) 5775–5798, https://doi.org/10.1007/s11661-018-4870-2.

[87] D.-E. Radulescu, O.R. Vasile, E. Andronescu, A. Ficai, Latest research of doped hydroxyapatite for bone tissue engineering, Int. J. Mol. Sci. 24 (2023), https://doi.org/10.3390/ijms241713157.

[88] M.S. Dwijaya, M.S. Utomo, G. Senopati, F. Rokhmanto, T. Asmaria, The effect of surface roughness on hydroxyapatite deposition on titanium alloys. AIP Conf. Proc, AIP Publishing, 2024.

[89] L.R. Bernal-Alvarez, C.F. Ramirez-Gutierrez, O.M. Gomez-Vazquez, B.A. Correa-Piña, L.F. Zubieta-Otero, B.M. Millán-Malo, M.E. Rodriguez-Garcia, Enhancing surface chemistry and wetting behavior of laser-modified Ti–6Al–4V surgical titanium alloy surfaces through wet deposition of biogenic hydroxyapatite, Surf. Coat. Technol. 489 (2024) 131065.

[90] D. Kuczyńska-Zemła, J. Pura, B. Przybyszewski, M. Pisarek, H. Garbacz, A comparative study of apatite growth and adhesion on a laser-functionalized titanium surface, Tribol. Int. 182 (2023) 108338.